

Configurational Temperatures and Interactions in Charge-Stabilized Colloid

Yilong Han

Department of Physics and Astronomy, University of Pennsylvania, 209 South 33rd St., Philadelphia, PA 19104

David G. Grier

Department of Physics and Center for Soft Matter Physics,
New York University, 4 Washington Place, New York, NY 10003

(Dated: November 10, 2018)

A system's temperature can be defined in terms of its constituents' instantaneous positions rather than their momenta. Such configurational temperature definitions offer substantial benefits for experimental studies of soft condensed matter systems, most notably their applicability to overdamped systems whose instantaneous momenta may not be accessible. We demonstrate that the configurational temperature formalism can be derived from the classical hypervirial theorem, and introduce a hierarchy of hyperconfigurational temperature definitions, which are particularly well suited for experimental studies. We then use these analytical tools to probe the electrostatic interactions in monolayers of charge-stabilized colloidal spheres confined by parallel glass surfaces. The configurational and hyperconfigurational temperatures, together with a novel thermodynamic sum rule, provide previously lacking self-consistency tests for interaction measurements based on digital video microscopy, and thereby cast new light on controversial reports of confinement-induced like-charge attractions. We further introduce a new method for measuring the pair potential directly that uses consistency of the configurational and hyperconfigurational temperatures as a set of constraints for a model-free search.

I. GENERALIZED TEMPERATURE DEFINITIONS

A variety of thermodynamic temperature definitions complementary to the classic kinetic definition have been derived recently [1, 2, 3]. The most general form, proved in Ref. [3] and [4], is:

$$k_B T = \frac{\langle \nabla \mathcal{H}(\mathbf{\Gamma}) \cdot \mathbf{B}(\mathbf{\Gamma}) \rangle}{\langle \nabla \cdot \mathbf{B}(\mathbf{\Gamma}) \rangle}, \quad (1)$$

where $\mathbf{\Gamma} = \{\Gamma_1, \dots, \Gamma_{6N}\} = \{q_1, \dots, q_{3N}, p_1, \dots, p_{3N}\}$ is the set of $3N$ generalized coordinates q_i and $3N$ conjugate momenta p_i describing the $6N$ -dimensional phase space of an N -particle system in equilibrium, and angle brackets $\langle \dots \rangle$ represent an ensemble average. The system's Hamiltonian, $\mathcal{H}(\mathbf{\Gamma}) = K(\{p_i\}) + V(\{q_i\})$, consists of the potential energy $K(\{p_i\}) = \sum_{i=1}^{3N} p_i^2 / (2m)$ and the conservative N -body potential $V(\{q_i\})$. The most noteworthy feature of Eq. (1) is that $\mathbf{B}(\mathbf{\Gamma})$ can be *any* continuous and differentiable vector in phase space [4]. Choosing $\mathbf{B}(\mathbf{\Gamma}) = \{0, \dots, 0, p_1, \dots, p_{3N}\}$ yields the familiar equipartition theorem,

$$k_B T = \left\langle \frac{1}{N} \sum_{j=1}^N \frac{p_j^2}{m_j} \right\rangle, \quad (2)$$

where m_j is the mass of the j -th particle. Choosing instead $\mathbf{B}(\mathbf{\Gamma}) = -\nabla V(\{q_i\})$ yields

$$k_B T_{config} = \frac{\langle \nabla V \cdot \nabla V \rangle}{\langle \nabla^2 V \rangle}, \quad (3)$$

which depends only on the objects' positions and not their momenta. This has come to be called the configurational temperature.

The configurational temperature's independence of the particles' momenta has important ramifications for experimental studies of systems such as colloidal suspensions whose configurations are easily measured but whose momenta are not. The experiments described in this Article exploit properties of the configurational temperature to obtain new insights into the interactions between charge stabilized colloidal particles. When combined with thermodynamic sum rules, this formalism provides previously lacking thermodynamic self-consistency tests for measurements of the particles' effective pair potentials. The same formalism also can be used to measure pair potentials in soft-matter systems directly, thereby bypassing questions of interpretation raised in previous studies, and yielding comparably accurate results with substantially less data.

Section II provides an overview of several consequences of Eq. (1). These are extended in Sec. III to a hierarchy of hyperconfigurational temperatures that lend themselves particularly nicely to experimental studies. Section IV provides an alternate foundation for the entire configurational temperature formalism in the classical hypervirial theorem. Consistency among the myriad temperature definitions is possible only if the assumptions underlying their derivations all are satisfied simultaneously. Applying these definitions to experimental data, as described in Sec. V, therefore probes the nature of the system's interparticle interactions. These data were obtained from digital video microscopy measurements on monolayers of charge-stabilized colloidal spheres dispersed in water between parallel glass surfaces. Not only does this system lend itself naturally to computing the configurational temperature, but the results also help to resolve a long-standing controversy regarding the nature of charged col-

loids' interactions in confined geometries. These results are summarized in Sec. VI.

II. CONFIGURATIONAL TEMPERATURES

The most general configurational temperature definition, Eq. (3), requires knowledge of the full N -body potential, which typically is not known for experimental systems. A more experimentally accessible form emerges if the particles interact via pairwise additive potentials, $u_{ij}(\mathbf{r}_i - \mathbf{r}_j)$. In this case, we can interpret gradients of the N -body potential,

$$\begin{aligned} \nabla V(\{q_i\}) &= \left(\frac{\partial}{\partial q_1}, \dots, \frac{\partial}{\partial q_{3N}} \right) \sum_{i=1}^{N-1} \sum_{j=i+1}^N u_{ij}(\mathbf{r}_i - \mathbf{r}_j) \\ &= -(\mathbf{F}_1, \dots, \mathbf{F}_N) \end{aligned} \quad (4)$$

as components of the net force acting on each of the particles due to their interactions with their neighbors, where

$$\mathbf{F}_j = \nabla_j \sum_{i \neq j} u_{ij}(\mathbf{r}_i - \mathbf{r}_j) \quad (5)$$

is the force acting on the j -th particle. The temperature then may be written as [3]

$$k_B T_{conF} = \frac{\left\langle \sum_{j=1}^N \mathbf{F}_j^2 \right\rangle}{\left\langle -\sum_{j=1}^N \nabla_j \cdot \mathbf{F}_j \right\rangle}. \quad (6)$$

It makes sense that the temperature should be reflected in the instantaneous distribution of forces because objects explore more of their potential energy landscape as the temperature increases.

All definitions of the temperature derived from Eq. (1) involve approximations of $\mathcal{O}(1/N)$, and so only are valid in the thermodynamic limit, $N \rightarrow \infty$. Dropping additional terms of $\mathcal{O}(1/N)$ in the derivation of Eq. (6) can be justified for systems with short-ranged interactions and leads to another equivalent temperature definition [3]:

$$k_B T_{con1} = \left\langle \frac{\sum_{j=1}^N \mathbf{F}_j^2}{-\sum_{j=1}^N \nabla_j \cdot \mathbf{F}_j} \right\rangle. \quad (7)$$

Neglecting further higher-order terms yields still another form [5],

$$k_B T_{con2} = \left\langle \frac{-\sum_{j=1}^N \nabla_j \cdot \mathbf{F}_j}{\sum_{j=1}^N \mathbf{F}_j^2} \right\rangle^{-1}. \quad (8)$$

III. HYPERCONFIGURATIONAL TEMPERATURES

Choosing $\mathbf{B}(\Gamma) = \{q_1^s, \dots, q_{3N}^s, 0, \dots, 0\}$ with $s = 1, 2, 3 \dots$ in Eq. (1) yields a hierarchy of so-called hypervirial temperatures [6], which reduce to the Clausius's

virial temperature for $s = 1$. By the same token, we propose that $\mathbf{B}(\Gamma) = \{F_1^s, \dots, F_{3N}^s, 0, \dots, 0\}$ with $s > 0$, yields the set of "hyperconfigurational temperatures" [5],

$$k_B T_h^{(s)} = \frac{\left\langle \sum_{i=1}^{3N} F_i^{s+1} \right\rangle}{\left\langle -s \sum_{i=1}^{3N} F_i^{s-1} \partial_i F_i \right\rangle}, \quad (9)$$

of which $T_h^{(1)}$ is equivalent to the standard configurational temperature. Here, F_i is the magnitude of the i -th element in the set of $3N$ components of the forces on the N particles. Because F_i is non-negative, $T_h^{(s)}$ is well defined for any positive real value of s . Negative values of s would yield diverging temperatures because at least some of the F_i will be vanishingly small for any system substantially larger than the range of interactions.

A simple example motivates introducing this new hierarchy of definitions. If, for example, a system is characterized by Coulomb pair interactions, $u(r) = 1/r$ in $d = 3$ dimensions, each term of the denominator, $\nabla_r^2 u(r) = r^{1-d} \partial_r(r^{d-1} \partial_r u(r))$, of Eqs. (6) and (7) vanishes. Consequently, the associated configurational temperature definitions in Eqs. (6), (7) and (8) diverge unphysically. The hyperconfigurational temperatures, by contrast, are still well defined with $\partial_x F_x = (1 - 3x^2/r^2)/r^3$, and $F_x^{s-1} \partial_x F_x + F_y^{s-1} \partial_y F_y + F_z^{s-1} \partial_z F_z \neq 0$ for $s \neq 1$. Consequently, the hyperconfigurational temperatures should apply to any system whose pair potential is continuous and differentiable. This suggests that they will be useful for studying systems whose interactions are not known *a priori*.

Additional useful results emerge for systems such as colloidal monolayers whose interactions are isotropic. In this case, the Cartesian coordinates may be analyzed independently

$$\begin{aligned} k_B T_{conF} &= \frac{\left\langle \sum_{j=1}^N \mathbf{F}_j^2 \right\rangle}{\left\langle -\sum_{j=1}^N \nabla_j \cdot \mathbf{F}_j \right\rangle} = \frac{\left\langle \sum_{j=1}^N (F_{j,x}^2 + F_{j,y}^2) \right\rangle}{\left\langle -\sum_{j=1}^N (F'_{j,x} + F'_{j,y}) \right\rangle} \\ &= \frac{\left\langle \sum_{j=1}^N F_{j,x}^2 \right\rangle}{\left\langle -\sum_{j=1}^N F'_{j,x} \right\rangle} = \frac{\left\langle \sum_{j=1}^N F_{j,y}^2 \right\rangle}{\left\langle -\sum_{j=1}^N F'_{j,y} \right\rangle}. \end{aligned} \quad (10)$$

Setting $\mathbf{B}(\Gamma) = \partial_x V(\{q_i\})$ or $\partial_y V(\{q_i\})$ in Eq. (1) leads to same results. We will refer to the two terms in Eq. (10), as well as analogous results for other temperature definitions, as the Cartesian components of the configurational temperature, T_x and T_y , respectively.

IV. DERIVATION FROM THE HYPERVIRIAL THEOREM

A remarkable consequence of Eq. (1) is that *any* vector field $\mathbf{B}(\Gamma)$ that depends only on the $3N$ configurational degrees of freedom gives rise to a functionally distinct but

thermodynamically equivalent definition of the temperature that depends only on configurational coordinates. Here we show that this insight emerges transparently from the hypervirial theorem [6, 7], and that Eq. (1) itself can be derived from this starting point.

The Hamiltonian equation of motion for an arbitrary dynamical variable, $f(\mathbf{\Gamma}, t)$, is

$$\frac{df}{dt} = \frac{\partial f}{\partial t} + \{f, \mathcal{H}(\mathbf{\Gamma})\}, \quad (11)$$

where

$$\{f, \mathcal{H}(\mathbf{\Gamma})\} = \sum_{i=1}^{3N} \left[\frac{\partial \mathcal{H}(\mathbf{\Gamma})}{\partial p_i} \frac{\partial f}{\partial q_i} - \frac{\partial \mathcal{H}(\mathbf{\Gamma})}{\partial q_i} \frac{\partial f}{\partial p_i} \right] \quad (12)$$

is the Poisson bracket of f and $\mathcal{H}(\mathbf{\Gamma})$. Provided that (1) f does not depend explicitly on time and (2) $f(\mathbf{\Gamma})$ remains bounded in the course of time, the time average of Eq. (11) yields the classical hypervirial theorem,

$$\langle \{f, \mathcal{H}(\mathbf{\Gamma})\} \rangle = 0 \quad (13)$$

or, equivalently,

$$\sum_{i=1}^{3N} \left\langle \frac{\partial \mathcal{H}(\mathbf{\Gamma})}{\partial p_i} \frac{\partial f}{\partial q_i} \right\rangle = \sum_{i=1}^{3N} \left\langle \frac{\partial \mathcal{H}(\mathbf{\Gamma})}{\partial q_i} \frac{\partial f}{\partial p_i} \right\rangle. \quad (14)$$

If we restrict f to be a homogeneous first-degree function of the momenta,

$$f(\mathbf{\Gamma}) = p_j Q(\{q_i\}), \quad (15)$$

while still allowing Q to be an arbitrary function of coordinates, the right hand side of Eq. (14) becomes

$$\sum_{i=1}^{3N} \left\langle \frac{\partial \mathcal{H}(\mathbf{\Gamma})}{\partial q_i} \frac{\partial f}{\partial p_i} \right\rangle = \left\langle Q \frac{\partial \mathcal{H}(\mathbf{\Gamma})}{\partial q_j} \right\rangle = \left\langle Q \frac{\partial V(\{q_i\})}{\partial q_j} \right\rangle. \quad (16)$$

The coordinates and momenta are statistically uncorrelated in equilibrium, so that

$$\sum_{i=1}^{3N} \left\langle \frac{\partial \mathcal{H}(\mathbf{\Gamma})}{\partial p_i} \frac{\partial f}{\partial q_i} \right\rangle = \sum_{i=1}^{3N} \left\langle \frac{\partial \mathcal{H}(\mathbf{\Gamma})}{\partial p_i} p_j \right\rangle \left\langle \frac{\partial Q}{\partial q_i} \right\rangle \quad (17)$$

$$= \left\langle p_i \frac{\partial \mathcal{H}(\mathbf{\Gamma})}{\partial p_i} \right\rangle \left\langle \frac{\partial Q}{\partial q_i} \right\rangle, \quad (18)$$

where terms with $i \neq j$ vanish. Now, $\left\langle p_i \frac{\partial \mathcal{H}(\mathbf{\Gamma})}{\partial p_i} \right\rangle = k_B T$ is the standard kinematic definition of the temperature. Substituting this, Eq. (16) and Eq. (18) into Eq. (14) yields

$$k_B T = \left\langle Q \frac{\partial V(\{q_i\})}{\partial q_j} \right\rangle \left\langle \frac{\partial Q}{\partial q_i} \right\rangle^{-1}, \quad (19)$$

which is a special case of Eq. (1) when $\mathbf{B}(\mathbf{\Gamma}) = \mathbf{B}(\{q_i\})$.

Hirschfelder [6] chose $Q = q_i^s$ to obtain a hierarchy of hypervirial temperatures characterized by the index s .

Choosing instead $Q = F_i^s$ yields the hyperconfigurational temperatures in Eq. (9).

A similar line of reasoning provides a straightforward derivation of the most general result, Eq. (1). We begin by choosing $Q = q_i$ in Eq. (19) to obtain $k_B T = \left\langle q_i \frac{\partial \mathcal{H}(\mathbf{\Gamma})}{\partial q_i} \right\rangle$, which is equivalent to the Clausius virial theorem, $k_B T = \langle r_i F_i \rangle$, for systems with pairwise additive interactions. Next, we choose $f(\mathbf{\Gamma}) = q_i P(\{p_i\})$, where P is an arbitrary function of the momenta, and substitute into Eq. (14). The following steps are analogous to those used in deriving Eq. (19) and yield

$$k_B T = \left\langle P \frac{\partial K(\{p_i\})}{\partial p_j} \right\rangle \left\langle \frac{\partial P}{\partial p_i} \right\rangle^{-1}. \quad (20)$$

Combining this with Eq. (19) yields

$$k_B T = \frac{\left\langle Q P \left(\frac{\partial V(\{q_i\})}{\partial q_i} + \frac{\partial K(\{p_i\})}{\partial p_i} \right) \right\rangle}{\left\langle P \frac{\partial Q}{\partial q_i} + Q \frac{\partial P}{\partial p_i} \right\rangle} \quad (21)$$

$$= \frac{\langle Q P \nabla_i \mathcal{H}(\mathbf{\Gamma}) \rangle}{\nabla_i (Q P)}, \quad (22)$$

where, once again, we have exploited the statistical independence of the coordinates and momenta. Because this holds for any choice of Q and P , it holds for any sum of products of the form $\sum_m Q_m P_m$. Thus, Eq. (22) is equivalent to Eq. (1) for any choice of $\mathbf{B}(\mathbf{\Gamma})$ whose components can be expressed as Taylor series in the coordinates and momenta.

V. APPLICATION TO COLLOIDAL DISPERSIONS

Because the positions of microscopic particles, such as atoms, are hard to measure, experimental applications of the configurational temperature have been relatively limited [5]. Colloidal dispersions differ from many experimental systems in that their constituents' motions can be tracked quite easily. Unlike most macroscopic model systems, they can be thoroughly equilibrated through the particles' intimate contact with the suspending fluid. Furthermore, an effective potential between two particles often can be defined. For this reason, colloidal dispersions offer an almost ideal experimental test-bed for studying the configurational temperature and related ideas. These ideas, in turn, provide valuable new tools for assessing the microscopic state of this important state of matter.

This section describes methods for estimating the configurational and hyperconfigurational temperatures of colloidal dispersions from digital video microscopy measurements of their microscopic dynamics. Emphasis is placed on how to account for inevitable experimental errors in systems of limited size whose interactions may not be fully characterized *a priori*. In particular, we analyze the structure and dynamics of dilute monolayers of

charge-stabilized colloidal spheres confined by planar surfaces, on the one hand using convergence of different temperature definitions as a thermodynamic self-consistency test for independently measured effective pair potentials, and on the other as a new approach to measuring the pair potential directly.

A. Interactions in charge-stabilized colloid

Considerable attention has been focused in recent years on colloidal interactions, particularly in light of experimental observations that challenge theoretical predictions. For example, charged colloidal spheres of diameter σ and charge number Z dispersed in an electrolyte interact with each other directly through their Coulomb repulsion and also indirectly through their influence on the surrounding distribution of simple, atomic-scale ions. Poisson-Boltzmann mean-field theory predicts an overall screened-Coulomb repulsion [8] of the form

$$\beta u(r) = Z^2 \lambda_B \frac{\exp(\kappa\sigma)}{\left(1 + \frac{\kappa\sigma}{2}\right)^2} \frac{\exp(-\kappa r)}{r}, \quad (23)$$

where $\beta^{-1} = k_B T$ is the thermal energy scale at absolute temperature T , r is the spheres' center-to-center separation, and $\lambda_B = e^2/(4\pi\epsilon k_B T)$ is the Bjerrum length in a medium of dielectric constant ϵ . If the electrolyte has a *total* concentration c of monovalent ions, then the Debye-Hückel screening length, $\kappa^{-1} = 1/\sqrt{4\pi\lambda_B c}$, sets the range of the effective electrostatic interaction in the mean-field approximation. This is an effective interaction because it results from an average over the simple ions' degrees of freedom. When viewed in this light, it is not surprising that measurements might differ from predictions based on Eq. (23). More surprising is that like-charged colloidal spheres appear to *attract* each other under some circumstances, in qualitative disagreement with Eq. (23). One of the goals of the present study is to apply the configurational temperature formalism to resolve some of the outstanding questions regarding these anomalous like-charge attractions.

Unlike atoms, which travel ballistically within the potential energy landscape established by inter-atomic interactions, colloidal particles are immersed in a viscous fluid that randomizes their trajectories over intervals longer than $\tau = \beta m D$, the momentum relaxation time. Given a typical colloidal diffusion coefficient $D \approx 1 \mu\text{m}^2/\text{sec}$, $\tau \approx 1 \mu\text{sec}$. Consequently colloidal suspensions' microscopic temperatures are not easily monitored with the usual kinetic definition of the temperature, Eq. (2). The configurational temperature, by contrast, can be measured from snapshots and so provides an ideal alternative.

The fluid also acts as an intimately coupled heat bath whose heat capacity vastly exceeds the colloidal particles'. Consequently, the dispersion's thermodynamic temperature is all but guaranteed to be the fluid's, which

is readily monitored with standard techniques. It is natural, therefore, to compare estimates of the configurational temperature based on microscopic dynamical measurements with this bulk thermodynamic temperature.

Our samples consist of negatively charged silica spheres $\sigma = 1.58 \mu\text{m}$ in diameter (Duke Scientific Lot. 24169) dispersed in water and confined within a slit pore of height H formed between a glass microscope slide and a cover slip. The glass surfaces also develop large negative charge densities in contact with water [9], which repel the spheres and prevent them from sticking under the influence of van der Waals attraction. Silica spheres are roughly twice as dense as water and sediment onto the lower wall in a matter of seconds. The low-concentration samples used in this study thus form a dilute monolayer once they reach equilibrium. Reservoirs of mixed-bed ion exchange resin help to maintain a total ionic strength around $c = 5 \times 10^{-6} \text{ M}$ in the $1 \times 4 \text{ cm}^2$ visible sample area.

The hermetically sealed sample is allowed to equilibrate at ambient temperatures on the stage of a microscope. The particles' motions are imaged with a CCD (charge-coupled device) camera and video taped at 30 frames/sec before being digitized. Standard methods of digital video analysis [10] identify the particles in each video frame and report their locations in the plane with a resolution of 30 nm. The resulting distribution,

$$\rho(\mathbf{r}, t) = \sum_{j=1}^{N(t)} \delta(\mathbf{r} - \mathbf{r}_j(t)), \quad (24)$$

of $N(t)$ particles in the field of view at time t provides detailed information regarding the particles' dynamics under the combined influences of random thermal forces and their mutual interactions. Distilling this information into an easily interpreted form requires further analysis.

One of the most commonly used tools for analyzing colloidal microscopy data is the radial distribution function, $g(r)$, which is computed as

$$g(r) = \frac{1}{n^2} \langle \rho(\mathbf{r} - \mathbf{r}', t) \rho(\mathbf{r}', t) \rangle, \quad (25)$$

where $n = \langle \rho \rangle = N/A$ is the areal density of particles in a field of view containing $N = \langle N(t) \rangle$ particles. Angle brackets in Eq. (25) denote averages over both angle and time. A typical example appears in the inset to Fig. 1.

B. Colloidal interaction measurements

For a system with radially symmetric pairwise-additive interactions, the radial distribution function can be related to the pair potential, $u(r)$. As a starting point, we introduce the potential of mean force,

$$w(r) \equiv -k_B T \ln g(r), \quad (26)$$

which reduces to the pair potential in the dilute limit: $\lim_{n \rightarrow 0} w(r) = u(r)$. Crowding at higher concentrations

induces many-body correlations that appear as oscillations both in $g(r)$ and also in $w(r)$. Such oscillations arise even in systems with monotonically repulsive interactions, and could be mistaken for structure in $u(r)$. Reducing the concentration to avoid many-body correlations often is not practical given the competing requirements of tracking particles accurately (which favors high magnifications [11]) and amassing adequate statistics in $g(r)$ (which favors a wide field of view and thus low magnification [12]).

No exact closed-form relationship between $g(r)$ and $u(r)$ is known for systems at finite concentrations. Fortunately, Henderson's uniqueness theorem [13] guarantees that any trial potential that reproduces $g(r)$ uniquely describes the system's interactions, provided these are indeed pairwise additive. In light of this, two complementary methods for inverting $g(r)$ to obtain $u(r)$ have been introduced. The inverse Brownian dynamics [14] and inverse Monte Carlo [15] techniques compare the experimental radial distribution function with results obtained from numerical simulations based on experimental conditions and trial potentials until a match is obtained. The liquid structure inversion technique [16] uses the Ornstein-Zernike (OZ) integral equation [17] to correct for many-body correlations directly. This is the approach we will adopt.

The OZ equation describes the evolution of many-body correlations from a hierarchy of pairwise interactions. Truncating the hierarchy yields approximate but analytically tractable relationships between $g(r)$ and $u(r)$. Among these, the hypernetted chain (HNC) approximation is found to be accurate for “soft” potentials while the Percus-Yevick (PY) approximation is more accurate for short-ranged interactions. For two-dimensional systems, the pair potential can be evaluated in these approximations as [18]

$$u(r) = w(r) + \begin{cases} k_B T n I(r) & \text{(HNC)} \\ k_B T \ln(1 + n I(r)) & \text{(PY)} \end{cases} \quad (27)$$

where the convolution integral,

$$I(r) = \int_A [g(r') - 1 - nI(r)] [g(|\mathbf{r}' - \mathbf{r}|) - 1] d^2 r', \quad (28)$$

is solved iteratively, starting with $I(r) = 0$.

Provided the particles' concentration is not too high, and that their interactions are pairwise additive and neither too long-ranged nor too short, and that $g(r)$ is known with sufficient accuracy, both approximations should yield equivalent results for $u(r)$. Unfortunately, consistency does not guarantee accuracy [12], and additional checks are necessary to ensure that pair potentials obtained with Eqs. (27) and (28) are meaningful. This is all the more important if such measurements as the example in Fig. 1, run counter to long-established theory [19]. In this particular case, the $0.3 k_B T$ deep minimum at $r = 1.5 \sigma$ is inconsistent with the purely repulsive

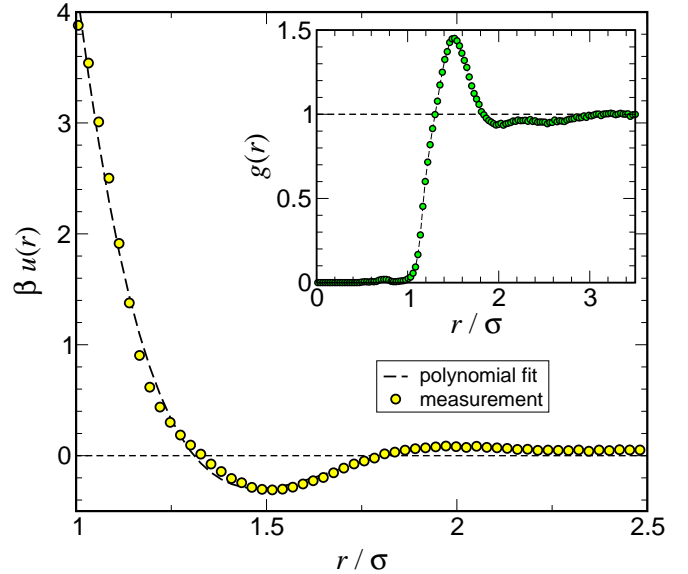


FIG. 1: Inset: Radial distribution function $g(r)$ for a monolayer of $\sigma = 1.58 \mu\text{m}$ diameter silica spheres sedimented onto a layer at areal density $n\sigma^2 = 0.0684$ above a glass surface in a parallel-plate slit pore of height $H = 9 \mu\text{m}$. Main plot: Effective pair potential obtained from $g(r)$ using Eqs. (27) and (28). The smooth dashed curve is a fifth-order polynomial fit.

interaction described by Eq. (23). Such anomalous interactions have been reported before in confined colloidal monoayers [14, 16, 19, 20], but their origin has remained unresolved for more than a decade. Is this minimum a real albeit unexplained feature of the charged colloids' pair interaction, or is it an artifact of the measurement technique?

C. Temperature-based consistency tests for $u(r)$

Because hyperconfigurational temperatures depend sensitively on particles' interactions, they constitute a hierarchy of thermodynamic self-consistency tests for $u(r)$. The first successful application of the configurational temperature formalism to colloidal interaction measurements was reported in Ref. [5]. Here, we provide a more detailed description of these tests' implementation and compare their results with those from thermodynamic sum rules. Together, this suite of independent tests confirms that pair potentials extracted from digital video analysis of confined charge-stabilized colloidal monolayers can be both thermodynamically self-consistent and accurate.

The flow chart in Fig. 2 outlines our strategy for checking and optimizing pair potentials. Given a candidate pair potential, we calculate a variety of configurational temperatures and compare these with the known bulk temperature at which the experiment was performed. Equation (27) conveniently yields $u(r)$ in units of $k_B T$, so that configurational temperatures derived from $u(r)$ are

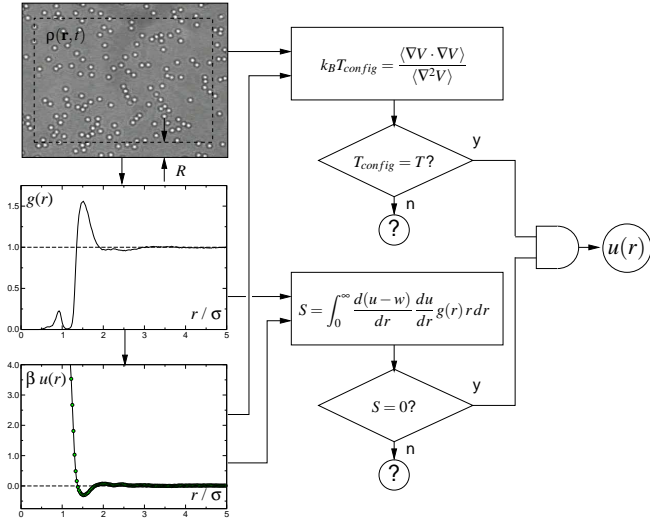


FIG. 2: Flow chart for applying configurational temperatures to colloidal interaction measurements. From the measured positions of particles, $\rho(\mathbf{r}, t)$, we can calculate the radial distribution function $g(r)$ and, from this, the candidate pair potential, $u(r)$. $\rho(\mathbf{r}, t)$ and $u(r)$ are used to calculate the configurational temperatures, while $g(r)$ and $u(r)$ are used to compute the sum rule in Eq. (32). Thermodynamic self-consistency in both tests suggests that $u(r)$ accurately describes equilibrium pair-wise interactions in the system. Data were obtained for a sample at $H = 18 \mu\text{m}$.

automatically normalized by the bulk thermodynamic temperature, T . The condition for thermodynamic consistency therefore reduces to $T_{config} = 1$ in these units. Successful collapse of the hierarchy of configurational temperatures to the thermodynamic temperature suggests that all of the conditions assumed in the configurational temperatures' derivations have been met and that $u(r)$ accurately describes pairwise additive contributions to the free energy of a homogeneous isotropic system in equilibrium. Conversely, a failure to converge suggests that one or more of these conditions has not been met.

Identifying departures from equilibrium is particularly important in experimental systems where subtle fluid flows or environmental drifts can lead to correlations that might be mistaken for intrinsic interactions. Numerical simulations have demonstrated that the configurational temperature tracks sudden temperature jumps [2] far faster than the pressure or internal energy, and that its fluctuations also decay more rapidly, particularly for shorter-ranged potentials [21]. These observations suggest that the configurational temperature may converge to a well-defined value even before the system achieves equilibrium. This surprising insensitivity has been ascribed [21] to the dominant contribution to the configurational temperature of forces among nearby pairs of particles, which can relax to near-equilibrium configurations long before a disturbance can propagate through the entire system. The configurational temperature, therefore, is a better probe of local equilibrium than global.

D. A sum rule for interaction measurements

Thermodynamic sum rules provide the necessary tests for global equilibrium. A particularly convenient form may be derived from Eq. (7) if the pair potential is radially symmetric. In this case,

$$k_B T \langle \nabla_r^2 u(r) \rangle = \langle |\nabla_r u(r)|^2 \rangle, \quad (29)$$

and we can explicitly calculate the thermodynamic averages of both sides of this equation:

$$\begin{aligned} \langle \nabla_r^2 u(r) \rangle &= 2\pi n N \int_0^\infty \left(\frac{1}{r} \frac{du}{dr} + \frac{d^2 u}{dr^2} \right) r g(r) dr \\ &= 2\pi n N \left\{ \int_0^\infty \frac{du}{dr} g(r) dr + \frac{du}{dr} r g(r) \Big|_0^\infty \right. \\ &\quad \left. - \int_0^\infty \frac{du}{dr} \frac{d}{dr} (r g(r)) dr \right\} \\ &= 2\pi n N \int_0^\infty \frac{du}{dr} \frac{dg(r)}{dr} r dr, \end{aligned} \quad (30)$$

and

$$\langle |\nabla_r u(r)|^2 \rangle = 2\pi n N \int_0^\infty \left(\frac{du}{dr} \right)^2 g(r) r dr. \quad (31)$$

Combining these results yields the sum rule

$$\int_0^\infty \left(\frac{du(r)}{dr} - \frac{d \ln g(r)}{dr} \right) \frac{du(r)}{dr} g(r) r dr = 0. \quad (32)$$

This sum rule should apply at arbitrary areal densities for any system whose interactions can be described by a pairwise-additive central potential, $u(r)$. A similar result was obtained in Ref. [22] for three-dimensional systems.

Using the radial distribution function to average over pairs of particles removes any sensitivity to local structural variations, and thus focuses attention on global properties such as the degree of equilibration. Consequently, Eq. (32) complements the hierarchy of configurational temperature consistency checks.

E. Practical considerations

1. The range of interactions

These thermodynamic tests turn out to be exceedingly sensitive to imperfections in experimental data, and care is required to apply them meaningfully. For example, video microscopy data necessarily is restricted to a limited field of view, even if the sample itself is substantially larger. Particles near the edge of the field of view may have strongly interacting neighbors just out of sight whose contributions to their net force would be overlooked. The large apparently unbalanced forces due to this pernicious edge effect would grossly distort estimates

of the configurational temperature were they included in averages such as Eq. (6).

To avoid this, we calculate force distributions only for particles whose relevant neighbors all lie within the field of view. Such particles lie no closer than the interaction's range R to the edge of the field of view. We estimate R from $u(r)$ and $g(r)$ by computing

$$\frac{T(r)}{T} = 2\pi \frac{r}{\sigma} g(r) \frac{|\nabla \beta u(r)|^2}{\nabla^2 \beta u(r)}, \quad (33)$$

which heuristically describes an effective contribution to the configurational temperature of $2\pi r g(r)$ pairs of spheres interacting with potential $u(r)$ at range r [5]. A typical example appears in Fig. 3. This should be considered no more than a heuristic guide because it neglects three-particle correlations, which are known [21] to be important for estimating the temperature.

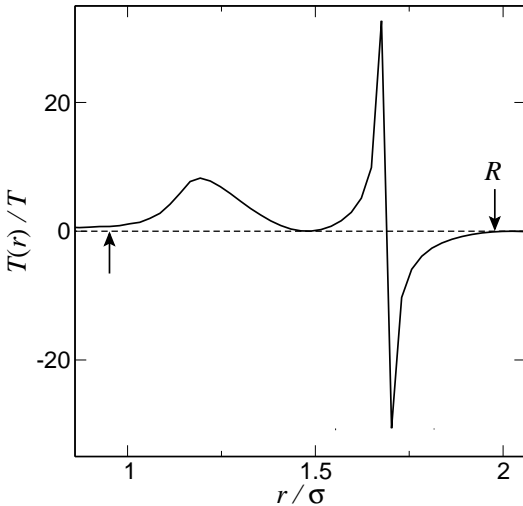


FIG. 3: Contributions to the configurational temperature due to pairs of colloidal spheres separated by distance r , calculated from the fifth-order polynomial fit to the data in Fig. 1. For this system, spheres separated by more than $R = 2\sigma$ contribute negligibly to the configurational temperature.

Pairs at large enough separation that their interactions are vanishingly weak contribute negligibly to $T(r)$. The interaction range R therefore can be estimated from the trailing edge of $T(r)$ in Fig. 3. By considering particles no closer than R to the edge of the field of view, we can ensure that no relevant pair interactions will be missed in calculating the full configurational temperature. The restricted field of view is indicated by the small rectangle overlaid on the photograph in Fig. 2. Given this cut on the data, we can proceed to calculate the full configurational temperature.

The data in Fig. 1 display two features whose validity we can assess using the configurational temperature formalism. The first is the anomalous minimum that can be interpreted as evidence for long-ranged attractions between like-charged particles. The second is the surprisingly weak contact repulsion. This low barrier to ag-

gregation probably is not real, otherwise particles would aggregate rapidly by van der Waals attraction. Could the minimum similarly be an artifact?

Closer inspection of the data in Fig. 1 reveals that $g(r)$ is finite even at $r < \sigma$, which should be impossible. Two sources of experimental error, projection error due to particles' small out-of-plane motions and polydispersity in the spheres' diameters, artificially increase $g(r)$ near contact and thus dramatically reduce the apparent interaction energy near $r = \sigma$. What Fig. 1 shows is the *effective potential* consistent with the raw data for the particles' positions $\rho(\mathbf{r}, t)$, including both of these contributions. The configurational temperature calculation also is based on the same raw position data and so requires the associated *effective potential* as an input. The consistency condition $T_{config} = 1$ thus tests the accuracy and thermodynamic self-consistency of $u(r)$ for the measured set of $\rho(\mathbf{r}, t)$ data.

Given $\rho(\mathbf{r}, t)$ and $u(r)$, the net force $\mathbf{F}_j(t)$ on the j -th particle at time t can be estimated using Eq. (5), with the sum over neighboring particles being restricted to those with $|\mathbf{r}_i - \mathbf{r}_j| \leq R$. The set of single-particle forces then can be compiled into estimates for the configurational temperature for that particular snapshot, and a sequence of snapshots averaged to obtain a final result. Averaging is not necessary if each snapshot captures a large enough number of particles. The dilute samples in our study, however, typically yield $N = \mathcal{O}(100)$ so that several thousand frames are required for adequate statistics.

2. Influence of measurement errors

Even when care is taken to avoid edge effects, naively calculating forces, and thus temperatures, with the experimentally sampled $u(r)$ yields unsatisfactory results, as the data in Fig. 4 demonstrate. This shows the histogram of T_{conF} values obtained from the 11912 video frames used to generate Fig. 1. Although the distribution is indeed peaked around unity, the average, $T_{conF} = 1155$, deviates wildly from the expected value. Other definitions also fare badly, with $T_{con1} = 23$, for example. These extraordinarily large averages are not representative of the force distribution, however. Rather, they can be ascribed to a small number of frames with huge apparent temperatures. More disturbingly, many frames appear to have negative temperatures.

Frames with negative temperature must have $\sum_i \nabla^2 u_j < 0$. The inset to Fig. 4 shows that this is indeed the case. Such negative values should be extraordinarily rare in an equilibrated system because they signal mechanical instability. In this case, however, they can be ascribed to scatter in the experimentally determined potential, $u(r)$, which is greatly emphasized by the Laplacian operator. Particularly for $r > 2\sigma$ where $u(r)$ is close to 0, the signal-to-noise ratio becomes small and errors in the computed configurational temperature

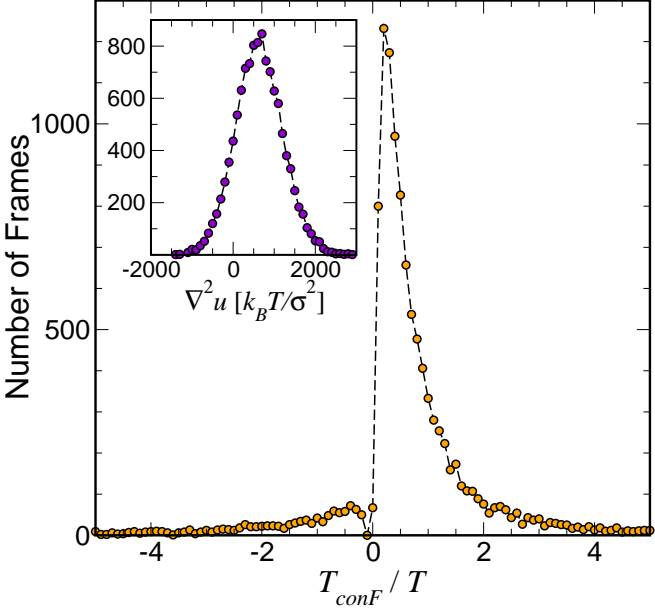


FIG. 4: Histogram of the configurational temperatures calculated from the measured pair potential in Fig. 1 with the interaction range $1 < r/\sigma < 10$ for a set of 11912 video frames, with an average of $N = 288$ particles per frame. Inset: corresponding histogram of $\sum_i \nabla^2 u_i$.

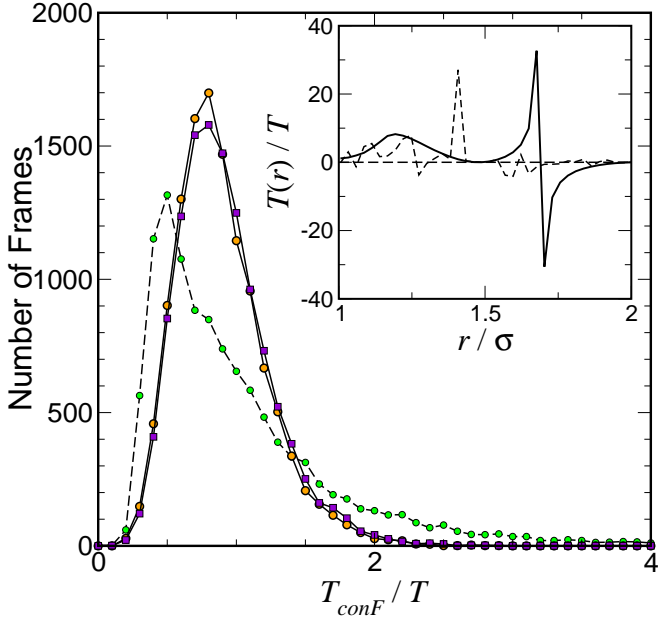


FIG. 5: Histogram of the configurational temperatures along the x and y directions calculated with the polynomial fit to the pair potential in Fig. 1. Solid curves: $T_{confF}^{(x)}$ (circles) and $T_{confF}^{(y)}$ (squares). Dashed curve: T_{confF} from raw $u(r)$. Inset: Contribution to the configurational temperature due to pairs at separation r for the measured $u(r)$ (dashed curve) and the polynomial fit to $u(r)$ (solid curve).

becomes unacceptably large. Cutting the long-range part

of $u(r)$ helps to some degree by substantially decreasing the number of frames with negative temperature. However, this does not suppress the high-temperature tail in the histogram of single-frame temperatures, as can be seen from the dashed plot in Fig. 5. These artifacts still boost the apparent temperature to an unrepresentative $T_{confF} = 1150$.

To minimize the influence of scatter in $u(r)$, we compute the configurational temperature using a fifth-order polynomial fit shown in Fig. 1 as the input potential. This simple smoothing procedure eliminates both negative and unreasonably large values of the calculated configurational temperature. The solid curves plotted in Fig. 5. show the resulting distribution of configurational temperatures factored along the orthogonal x and y directions in the field of view according to Eq. (10). The two component, $T_{confF}^{(x)}$ and $T_{confF}^{(y)}$ differ by less than 2.5%, which helps to confirm the system's isotropy. Their mean, $T_{confF} = 0.969$, also is reassuringly close to the expected value.

Even when the temperature is calculated with the smoothed pair potential, a few frames still have negative temperatures. This is reasonable if $\lim_{r \rightarrow \infty} u(r) = 0$ and the pair potential has an extremum at an intermediate separation, $0 < r_0 < R$. In this case $\nabla^2 u_j$ must change sign and some particles may contribute negative values to the average in a snapshot. Chances improve for the average itself to be negative if N is small. For example, 10 out of 11912 frames have negative apparent temperatures in a sample with $\langle N \rangle = 97$. Negative temperatures are not observed in samples characterized by purely repulsive interactions, such as the example introduced in Sec. V E 6.

3. Finite size scaling

The relatively small number of particles in the field of view has other ramifications. Because the various configurational temperature definitions involve different approximations of order $1/N$, we might expect their results to differ from each other and from the actual thermodynamic temperature accordingly. Imaging a substantially larger region of the sample is not feasible. On the other hand, deliberately sub-sampling the field of view allows us to probe the dependence on sample size, for which we can extrapolate the configurational temperatures to the thermodynamic limit.

The data in Fig. 6 were obtained by calculating the configurational temperature with the 640×480 pixel² field of view reduced by borders of 20, 40, 60, 80, 100, 120, 140, 160 and 180 pixels. The interaction range in this system is $R = 2\sigma = 14.9$ pixel. Reducing the number of particles in this manner substantially changes the estimated temperatures, thereby confirming the importance of finite-size scaling. We fit these results to polynomials in $1/N$ with statistical weighting estimated from the area and the interaction range. These weighted fits describe

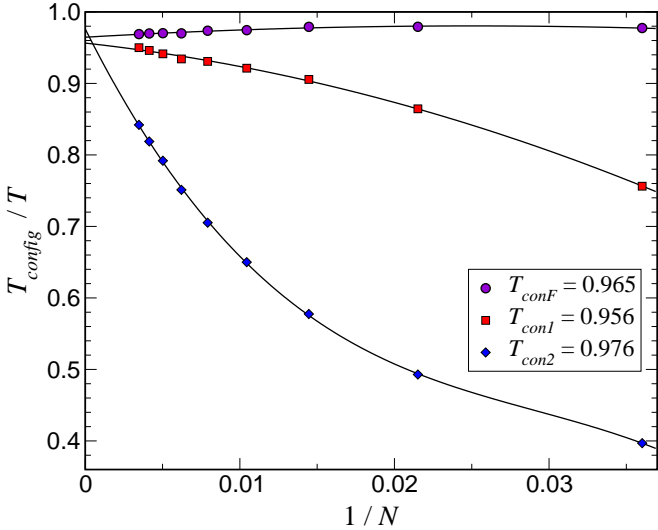


FIG. 6: Finite size scaling of T_{conF} , T_{con1} and T_{con2} for the data in Fig. 5, with area-weighted fits to second-, second- and third-order polynomials, respectively.

the data very well, so that the extrapolation to $1/N = 0$ should yield meaningful estimates for the configurational temperatures in the thermodynamic limit. Indeed, the extrapolated results, $T_{conF} = 0.965$, $T_{con1} = 0.956$ and $T_{con2} = 0.976$, agree quite well with each other, and all appear to be consistent with unity. Confirming thermodynamic consistency, however, requires us to assess the configurational temperatures' sensitivity to errors in $u(r)$.

4. Sensitivity to input potential

The apparently good extrapolation of the configurational temperatures to the thermodynamic temperature would offer little insight into the nature of the confined colloids' interactions if these results were insensitive to relevant features in the pair potential. For example, considerable attention has been paid in the literature to the possibility that anomalous confinement-induced like-charge attractions such as the example in Fig. 1 might be artifactual. However, if we truncate the negative region of $u(r)$ to create a purely repulsive potential and recalculate the configurational temperatures, T_{conF} , T_{con1} and T_{con2} all extrapolate to 1.5, an error of 150°C. The large deviation resulting from this admittedly crude test suggests that the observed attraction is indeed an integral part of the charged particles' interaction.

More sensitive tests for thermodynamic consistency are provided by the hyperconfigurational temperatures defined in Eq. (9). Figure 7 demonstrates how small variations in $u(r)$ can cause the hyperconfigurational temperatures to deviate with respect to each other and also with respect to the thermodynamic temperature. Two smoothed versions of the potential are plotted in

Fig. 7(a), one fit over the range $0.93 \sigma \leq r \leq R$ and the other over the more restricted $\sigma \leq r \leq R$. The former collapses the entire hierarchy of hyperconfigurational temperatures plotted in Fig. 7(b) to $\langle T_h^{(s)} \rangle \approx 1$ in the extrapolated thermodynamic limit, with $T_h^{(1)} = 1.012$, which compares favorably to $T_{conF} = 0.965$ in Fig. 6. The latter yields the far less satisfactory results in Fig. 7(c). Rather than collapsing onto the thermodynamic temperature, $T_h^{(s)}$ deviates systematically to lower values with larger index s .

This qualitative difference is due to substantial contributions from pairs of particles with $r < \sigma$. Such pairs should not be present in a monodisperse sample of impenetrable spheres, but appear in practice because of the sample's 3% polydispersity in radius and because of projection errors due to the particles' out-of-plane fluctuations. These two effects are responsible for the observed correlations at $r < \sigma$ in Fig. 1, and for the unreasonably small values of $u(r)$ in the unphysical range $0.5 \sigma < r < \sigma$. The successful collapse of the configurational and hyperconfigurational temperatures under these conditions demonstrates that the *effective* potential accounts for the apparent particle distribution $\rho(\mathbf{r})$ and may differ subtly from the *ideal* pair potential.

The results in Fig. 7(b) and 7(c) reflect the general trend that higher order hyperconfigurational temperatures are more sensitive to details of the input potential. Even so, we can adjust the input potential within the experimental error bounds so that all of the hyperconfigurational temperatures converge to unity. In this sense, the hyperconfigurational temperatures not only strengthen our conclusions regarding the nature of anomalous like-charge attractions, but also enable us to improve our estimates for $u(r)$ by adjusting for improved thermodynamic self-consistency.

The data in Fig. 7(c) also highlight another general feature of the configurational temperatures. Even though the more restricted trial potential does not successfully collapse the data, it does yield consistent results for configurational temperatures factored along orthogonal directions. This is a good indication that, indeed, the system is isotropic.

5. Checking for isotropy

Comparing temperatures measured along orthogonal directions not only provides a useful check for the interactions' isotropy, but also can be used to appraise the imaging system. For an isotropic sample, we expect that

$$\frac{\Delta T}{\langle T \rangle} \equiv 2 \frac{T_x - T_y}{T_x + T_y} \quad (34)$$

will vanish for *arbitrary* choices of $u(r)$. More usually, the combination of a commercial video camera and video

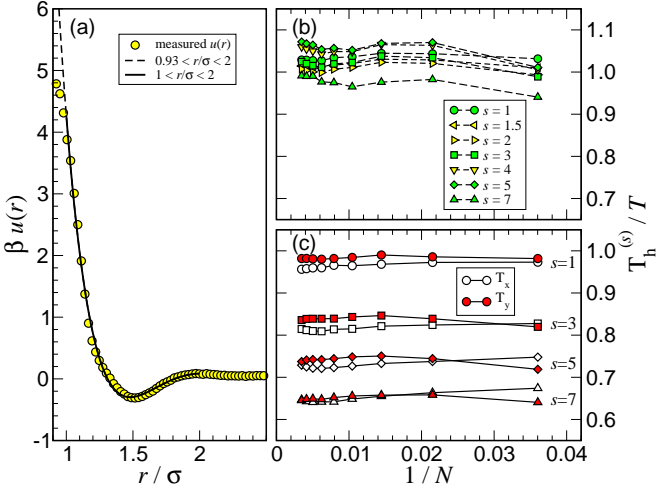


FIG. 7: (a) Measured pair potential $u(r)$ together with least-squares fits to fifth-order polynomials over the range $0.93 < r/\sigma < 2$ and $1 < r/\sigma < 2$. (b) Hyperconfigurational temperatures including data from $r < \sigma$. $T_h^{(1)} = 1.012$. (c) Hyperconfigurational temperatures over the more restricted range, factored into Cartesian components.

frame grabber results in slightly different length scale calibrations. Even quite small differences measurably affect the temperatures calculated from the associated force components if the interaction is assumed to be isotropic. For example, we found that $\Delta T = -0.025 \langle T \rangle$ for the confined sample at $H = 9$ and $\Delta T = 0.06 \langle T \rangle$ for the sample at $H = 195 \mu\text{m}$. Even such small differences are plainly visible in Fig. 7(c).

Apparent anisotropies of this magnitude appear consistently in our data sets regardless of the samples' composition, concentration, degree of confinement, and so are unlikely to reflect statistical errors. Nor are they likely to signal a real anisotropy in our samples' interactions. Instead, they result from the hyperconfigurational temperatures' sensitivity to subtle geometric distortion in our imaging system. Rescaling the measured x and y coordinates slightly can substantially reduce the apparent anisotropy in the entire hierarchy of hyperconfigurational temperatures, as the data in Table I show. For the system used in this study, a 0.7% correction of the $x : y$ scale ratio is enough to account for the 5.8% anisotropy of $T_h^{(1)}$ in the $H = 195 \mu\text{m}$ data.

The same scaling factor also corrects the apparent anisotropy in the other samples we have studied, and thus appears to be correctly interpreted as a correction to the calibration of our imaging system. Furthermore, differences in the scaling factors as small as $\pm 0.1\%$ perform substantially less well, as shown by the data in Table I. This level of sensitivity greatly exceeds the typical 1% calibration accuracy obtained by imaging test patterns, and thus provides a new tool for assessing and correcting geometric defects in the digital video microscopy system.

Successfully correcting apparent anisotropy in the hy-

$\frac{\Delta T}{\langle T \rangle}$	x : y scaling factor			
	1:1	1.003:0.997	1.003:0.9963	1.003:0.996
s	5.8%	0.61%	-0.07%	-0.82%
	4.4%	0.87%	0.009%	-0.20%
	2.6%	1.3%	0.16%	0.90%
	1.4%	1.8%	0.65%	0.71%

TABLE I: Correcting apparent anisotropy in the hyperconfigurational temperatures of the $H = 195 \mu\text{m}$ data set by rescaling coordinates. In each case, $g(r)$, $u(r)$ and $T_h^{(s)}$ were recalculated with revised particle locations.

perconfigurational temperatures also provides insight into the nature of the system's interactions. If replacing $u(r)$ by an arbitrary function causes T_x to differ from T_y then the system indeed may be anisotropic, either because its interactions are anisotropic, or else because of its response to an external field. In the latter case, the external field contributes an additional configuration-dependent term to the Hamiltonian, $\mathcal{H}_{ext}(\mathbf{r})$, which contributes, in turn, to the definitions of the configurational temperatures. If $\partial_x \mathcal{H}_{ext}(\mathbf{r}) \neq \partial_y \mathcal{H}_{ext}(\mathbf{r})$, then the configurational temperatures along the two directions generally will differ.

6. Accounting for sample imperfections in $T_h^{(s)}$

Colloidal samples quite often include small populations of aggregated pairs of spheres, also known as dimers. These can have a striking effect on the configurational temperature, as the data in Fig. 8 demonstrate. This sample also consists of $\sigma = 1.58 \mu\text{m}$ diameter silica spheres, but sedimented to the bottom wall of a slit pore $H = 195 \mu\text{m}$ thick at an areal density $n\sigma^2 = 0.080$. Unlike samples in relatively thin ($H = 9 \mu\text{m}$) slit pores considered so far, such weakly confined silica monolayers are found to have purely repulsive screened-Coulomb interactions [12, 19] in at least qualitative agreement with mean-field theory. The presence of a few dimers, however, contribute a small peak to the radial distribution function at $r = 0.8 \sigma$ whose tail extends to 1.1σ . These excess correlations are dramatically magnified in $T(r)/T$ because any two nominally repulsive particles ought to exert exceptionally large forces on each other near contact. The overall result is extremely large configurational temperatures.

At first glance, such defects in the sample would appear to render meaningful measurements of the configurational temperature impossible. However, the function $T(r)/T$ can be used to cut the spurious data while retaining enough useful information for an accurate assessment. In particular, the peak in $T(r)/T$ at small r is well separated from the principal peak at $r = 1.8 \sigma$. This suggests that the former can be ascribed entirely to dimers and the latter to genuine long-ranged interactions, with

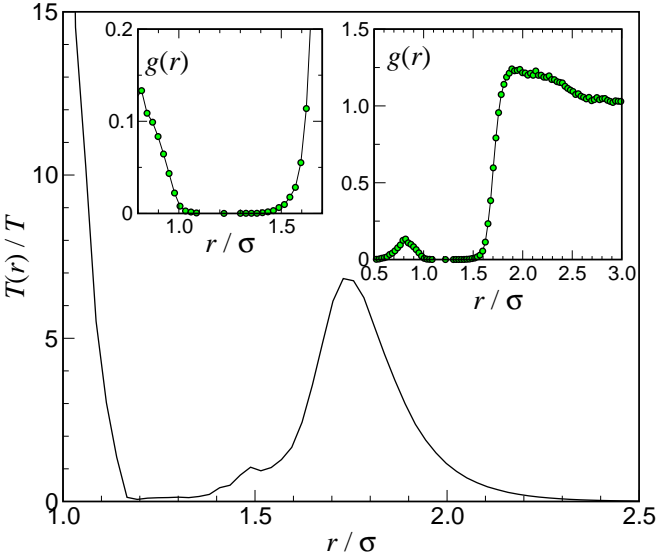


FIG. 8: Contribution to the configurational temperature at different pair separations assuming interactions described by Eq. (23) with $\kappa^{-1} = 180$ nm, $Z = 7563$ for a silica monolayer at $H = 195$ μm . The peak at $1 < r/\sigma < 1.2$ is caused by dimers. The tiny peak at $r = 1.5 \sigma$ is due to one particle stuck to the bottom surface. Right Inset: $g(r)$ with a dimer peak around $r = 0.8 \sigma$. Left Inset: a more detailed view of $g(r)$ near $r = \sigma$.

a clean division at about $r = 1.3 \sigma$. It seems reasonable, therefore, to eliminate dimers' contribution to the configurational temperatures by excluding any pair separations smaller than 1.3σ .

Restricting the range of $u(r)$ too much would exclude relevant interactions, causing the net force on many particles to appear unbalanced and the configurational temperature to increase accordingly. For the present data set, we find that increasing the lower cutoff to $r = 1.45 \sigma$ only increases the apparent temperature by a few percent. This indicates that three-body correlations are weak at this concentration range and that the proposed cutoff at $r = 1.3 \sigma$ will not distort the results. Similarly, ignoring contributions from pairs separated by more than $r = 2 \sigma$ has little influence on the estimated temperature and establishes the interaction range for accurate temperature estimates.

Figure 9 shows typical finite-size scaling results for a trial fourth-order polynomial fit to the experimentally obtained pair potential over the range $1.435 < r/\sigma < 1.89$. The fit potential is plotted as a dashed curve in Fig. 10(a). Replacing this with a fit to the predicted mean field potential described by Eq. (23) over the range $1.2 < r/\sigma < 1.95$ yields comparably good convergence, and increasing the range to $1.2 < r/\sigma < 10$ decreases the extrapolated configurational temperature by just 4 %. All of these trial potentials fall within error estimates for the measured potential. On this basis, and because the various definitions of the configurational temperature all extrapolate to unity, we conclude that the measured

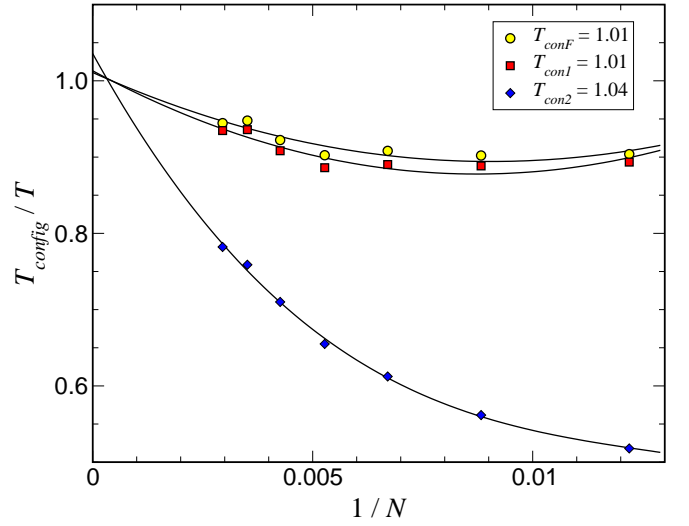


FIG. 9: Finite size scaling of three configurational temperature definitions computed for a purely repulsive monolayer of $\sigma = 1.58 \mu\text{m}$ silica spheres in a slit pore of height $H = 195 \mu\text{m}$. Solid curves are weighted fits to second-order polynomials in $1/N$ used to extrapolate to the thermodynamic limit. Data at $1/N < 0.005$ are influenced by the stuck particle, as discussed in the text.

potential once again accurately describes the system's equilibrium pair interactions. In this case, however, the potential appears to be purely repulsive.

The sample used to compile these data also included one particle that had deposited irreversibly onto the lower glass surface near the edge of the field of view. A single immobilized sphere might not be expected to influence the free monolayer's structure and dynamics much. The influence on the radial distribution function is indeed subtle, with the slight peak at $r = 1.5 \sigma$ in $T(r)/T$ (Fig. 8) disappearing when the region containing the stuck particle is excluded from the calculation. The effect on the candidate pair potential is somewhat more pronounced, particularly for $r < 1.5 \sigma$, as can be seen in Fig. 10(a). But does the potential from the restricted data set better reflect the system's interactions? After all, the configurational temperatures calculated with the unrestricted data in Fig. 9 all extrapolate reasonably well to the thermodynamic value. Figures 10(b) and 10(c) show that the hierarchy of hyperconfigurational temperatures collapses to unity only when the region containing the stuck particle is excluded. The restricted data set, therefore, offers a more accurate picture of the pair potential. This is consistent with our earlier observation that small uncertainties in $g(r)$ at small separations can be dramatically magnified in $u(r)$.

F. Applying the thermodynamic sum rule

Even when the configurational and hyperconfigurational temperatures converge to the thermodynamic

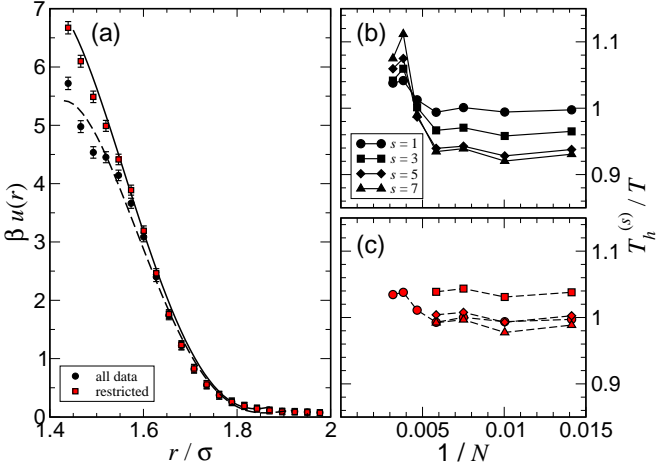


FIG. 10: Influence of an immobilized sphere on the effective pair potential and hyperconfigurational temperatures. (a) Measured pair potentials together with fourth-order polynomial fits yielding optimal collapse of the hyperconfigurational temperatures. Squares: results including all data. Circles: results obtained by excluding the region around the stuck sphere. (b) Hyperconfigurational temperatures obtained for the entire field of view. (c) Hyperconfigurational temperatures obtained for the restricted data set excluding the region around the stuck particle.

value for a reasonable choice of pair potential, the system's degree of equilibration still has to be assessed. Figure 11 shows the integrand of the sum rule in Eq. (32) for two slightly different effective potentials, both of which are consistent with the interactions measured in the confined colloidal monolayer at $H = 9 \mu\text{m}$. Even differences in the input potential too small to affect the configurational temperatures can change the sum rule's integrand substantially. These changes affect whether or not the sum rule as a whole is satisfied.

Normalizing the integral in Eq. (32) by the integral of the absolute value provides a useful measure of convergence. The best-fit pair potential obtained from the liquid structure inversion (plotted as circles in the inset to Fig. 11) yields an unacceptably large relative error of 0.5. At such low areal densities ($n\sigma^2 = 0.0684$), $u(r)$ is very similar to the potential of mean force, $w(r) = -k_B T \ln g(r)$, and very small changes in $u(r)$ can influence the sum rule's integrand substantially. In fact, adjusting the potential just slightly to the function plotted as squares in Fig. 11 improves the sum rule's convergence to 0.001. This modified potential still successfully collapses the configurational and hyperconfigurational temperatures, and thus may be considered an improved estimate for the pair potential. This successful application of the thermodynamic sum rule suggests that the system is indeed in equilibrium, and that the candidate pair potential, including its long-ranged attraction, accurately describes the confined particles' interactions.

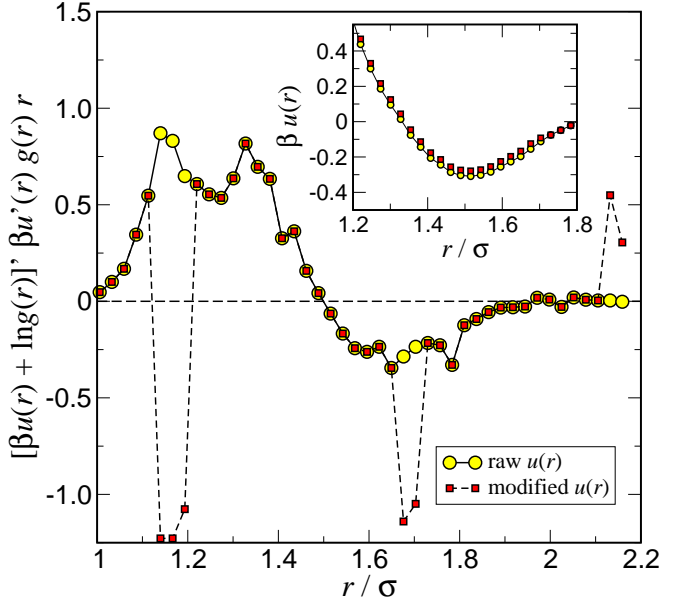


FIG. 11: Integrand of the sum rule in Eq. (32) for the confined silica monolayer at $H = 9 \mu\text{m}$. Inset: Best fit pair potential from Fig. 1 (circles) and another estimate (squares) consistent with both the confidence interval of $u(r)$ and with convergence of the configurational temperatures to the thermodynamic value. The former gives a relative error of 0.5 in the sum rule, and the latter 0.001.

G. Areal pressures

The foregoing considerations serve to confirm that the same colloidal silica spheres experience qualitatively different equilibrium pair interactions when confined between parallel glass walls separated by $H = 195 \mu\text{m}$ and $H = 9 \mu\text{m}$, with the more strongly confined dispersion exhibiting anomalous long-ranged attractions. Such a qualitative difference in the system's pair potential also should manifest itself in the system's other thermodynamic properties, such as its pressure.

Given the particles' locations and an estimate for their pair interactions, we can calculate the monolayers' pressure as $P = nk_B T + p^{pot}$, where p^{pot} is a departure from ideal gas behavior due to the particles' interactions. This so-called "potential pressure" is given by

$$Vp^{pot} = \frac{1}{d} \left\langle \sum_i \mathbf{r}_i \cdot \mathbf{F}_i \right\rangle = \frac{1}{d} \sum_{i < j} \mathbf{r}_{ij} \cdot \mathbf{F}_{ij} \quad (35)$$

where d is the dimension of the space, $\mathbf{r}_{ij} = \mathbf{r}_j - \mathbf{r}_i$ and $\mathbf{F}_{ij} = -\nabla_i u(\mathbf{r}_{ij})$. The former definition based on absolute coordinates works best for systems with open boundaries, which are described in the grand canonical ensemble, but fails in systems with periodic boundary conditions, which often are used in computer simulations. The latter definition based on relative coordinate works in both. Either should apply to our experimental data.

Comparing the different systems' interaction-driven

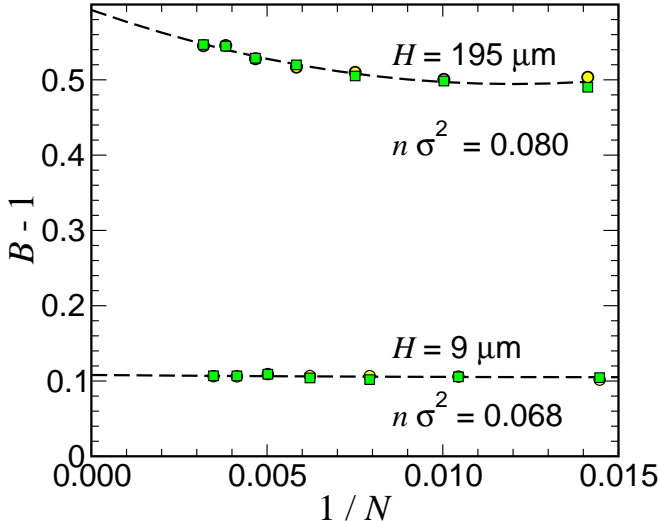


FIG. 12: Finite-size scaling of the normalized areal pressure for systems with repulsive and attractive potentials.

departures from ideal gas behavior is facilitated by defining

$$B = \frac{\beta P}{n} = 1 + \frac{\beta p^{pot}}{n}, \quad (36)$$

whose dependence on system size is plotted in Fig. 12. These data were obtained with the definition based on absolute coordinates measured from the center of the field of view. Equivalent results obtained with relative coordinates differ by less than 1.5%. As for the configurational temperature definitions, Eq. (35) applies in the thermodynamic limit, and B is obtained by extrapolating to large system size. In this case, we see that the system at $H = 195 \mu\text{m}$ with long-ranged repulsive interactions has a substantially higher pressure than would be expected for an ideal gas at the same areal density. The increase is much smaller in the more strongly confined system, presumably because of the potential's long-ranged attractive tail.

Like the configurational temperature, the pressure also depends sensitively on the input potential and length scale calibration. Without appropriate rescaling, P_x is 10% higher than P_y in the $H = 195 \mu\text{m}$ data set. After rescaling using the factors obtained by requiring isotropy in the configurational temperatures, the two components agree well, as can be seen in Fig. 12. This further confirms that the observed anisotropy is due to artificial image distortion that can be corrected with a single rescaling factor.

H. Using $T_h^{(s)}$ to measure $u(r)$

The configurational and hyperconfigurational temperatures show great promise as thermodynamic self-consistency tests for interaction measurements in soft-

matter system. They also can be used to measure interactions directly, with the hierarchy of definitions providing a set of simultaneous constraints on free parameters in a model for the pair potential. Even when the theoretical form of the potential is not known *a priori*, a numerically determined function that simultaneously collapses the entire hierarchy to the thermodynamic temperature would provide a model-free estimate for the potential.

As an example of this procedure, we use hyperconfigurational temperatures to determine the parameters κ^{-1} and Z in the screened-Coulomb potential, Eq. (23), that accounts for the distribution of particles in the $H = 195 \mu\text{m}$ data set [19]. Requiring $T_h^{(1)} = T_h^{(3)} = 1$ yields a screening length of $\kappa^{-1} = 208.4 \text{ nm}$ and an effective charge on the particles of $Z = 4123$. These values also converge $T_h^{(5)}$ and $T_h^{(7)}$ close to unity, suggesting that the screened-Coulomb potential reasonably describes the interactions in this system. Table II shows typical results for parameters near the optimal values.

Simply fitting Eq. (23) to the measured pair potential in Fig. 10(a) yields $\kappa^{-1} = 180 \pm 10 \text{ nm}$ and $Z = 6500 \pm 1000$. Although these values differ somewhat from those obtained by collapsing the configurational temperatures, both are broadly consistent with the charge regulation theory for interacting silica surfaces [9]. Their disagreement and the slight departure from unity of the highest-order hyperconfigurational temperatures suggests a small deviation of the true pair potential from the predicted screened-Coulomb form. This is reasonable because the nearby bottom wall probably affects the interaction somewhat. No convergence is possible at all for the data at $H = 9 \mu\text{m}$ because the pair interactions are not well described by the purely repulsive screened-Coulomb form.

Using hyperconfigurational temperatures to provide constraints on models for the pair potential offers advantages over other interaction measurement techniques. Principally, this method eliminates the intermediate steps of first measuring $g(r)$ and then inverting it to obtain $u(r)$. This first step generally requires amassing large amounts of data to obtain accurate information on correlations at small separations. The second involves uncontrolled approximations and limits the range of concentrations over which interactions can be measured. By contrast, the present approach requires substantially less data and involves fewer approximations. Consequently, this approach should be useful for exploring denser, more strongly interacting systems. Its ability to distinguish pairwise and many-body interactions also should be helpful for such studies.

On the other hand, calculating configurational temperatures involves sums over all pairs of particles, and must be repeated for sub-samples of varying size to account for finite-size scaling. This can be computationally expensive, particularly in model-free searches. Implementing fast search algorithms on restricted data sets with additional data being added only in the final stages of polishing should alleviate this problem.

κ^{-1} (nm)	Z	$T_h^{(1)}$	$T_h^{(3)}$	$T_h^{(5)}$	$T_h^{(7)}$
160	10147	1.00 ± 0.03	1.62 ± 0.12	1.53 ± 0.09	1.23 ± 0.06
180	6755	1.00 ± 0.02	1.31 ± 0.09	1.31 ± 0.07	1.08 ± 0.05
200	4779	1.00 ± 0.01	1.07 ± 0.07	1.12 ± 0.06	0.94 ± 0.04
210	4096	1.00 ± 0.01	0.98 ± 0.06	1.04 ± 0.06	0.88 ± 0.04
220	3549	1.00 ± 0.01	0.90 ± 0.05	0.96 ± 0.05	0.82 ± 0.04
250	2438	1.00 ± 0.01	0.72 ± 0.03	0.77 ± 0.04	0.68 ± 0.03

TABLE II: Determining the free parameters in a trial potential using $T_h^{(s)}$. Hyperconfigurational temperatures calculated from the screened-Coulomb potential for the $H = 195 \mu\text{m}$ data set over the range $1.3 < r/\sigma < 10$.

Failure of such a search to converge may signal a failure of pairwise additivity, a departure from equilibrium, or else an inappropriate model for the pair potential. Distinguishing these would probably require resorting to one of the alternate measurement methods.

VI. CONCLUSION AND DISCUSSION

The recently introduced notion of configurational temperature provides a valuable new tool for assessing experimental systems' thermodynamic state from static snapshots. We have introduced a hierarchy of hyperconfigurational temperatures that emerge naturally from the generalized definition of temperature, and have shown that both these and the generalized definition of the temperature can be derived from the classical hypervirial theorem. Colloidal monolayers provide an ideal experimental test bed for these new concepts in statistical mechanics.

We have tested the configurational and hyperconfigurational temperature to within 1% accuracy using particles' distribution and pair potentials measured in Ref. [19]. The effect of finite system size is clearly observed and accounted for in these measurements. Since the configurational temperatures' derivation requires pairwise additivity and their computation depends sensitively on the input potential, they can be used as thermodynamic self-consistency checks for measured pair potentials. The configurational temperatures calculated for our experimental data on confined colloidal silica monolayers confirm that our measured potentials are accurate and that they are consistent with the assumption of pairwise additivity.

We have found that higher-order hyperconfigurational temperatures are increasingly sensitive to errors in the potential $u(r)$ because of their dependence on higher moments of the force distribution. Even so, we have found that we can adjust the pair potentials within the measured uncertainties to converge the entire hierarchy of hyperconfigurational temperatures to unity for all of our data sets. This provides substantial independent evidence that our directly measured potentials reliably reflect equilibrium pair potentials for our systems.

A sum rule introduced in Sec. V D complements the information provided by the configurational and hyper-

configurational temperatures by providing additional insights into the system's degree of equilibration. Very small errors in the pair potential, moreover, are dramatically emphasized by the derivatives in the sum rule's definition. We find, nevertheless, that the sum rule can be satisfied for the colloidal samples in our study by adjusting the potential within the range of their uncertainties.

Applying these analytical tools to our system of sedimented colloidal silica spheres allows us to draw new conclusions regarding the nature of electrostatic interactions in this deceptively simple system. Rather than being purely repulsive, as mean-field theory predicts, confined colloids' interactions can be characterized by a strong and long-ranged attraction. This result echos those reported more than a decade ago in the first generation of colloidal interaction measurements [10, 14, 16, 23, 24]. Now, however, we can assert with confidence that the observed anomalous attractions constitute pairwise-additive contributions to the systems' equilibrium free energies, and not from any of the myriad of possible experimental artifacts that have been proposed. This interpretation is further bolstered by measurements of the areal pressure in these monolayers, which show clear signatures of their differing interactions. Resolving the anomaly of confinement-induced like-charge attractions therefore requires a fresh assessment of the nature of colloidal electrostatic interactions in simple electrolytes.

Hyperconfigurational temperatures also can be used as a set of constraints to determine the free parameters in a model for a system's pair interactions. We have demonstrated this by determining the two free parameters in a screened-Coulomb model for charge-stabilized colloids' interactions in the repulsive regime. In principle, the unbounded hierarchy of hyperconfigurational temperatures can be used in this way to determine any pairwise additive potential given the position, particularly if that potential can be modeled as a polynomial or comparably simple function.

One advantage of this method is that it circumvents the uncontrolled approximations that have dogged other approaches to measuring macroionic interactions in equilibrium. This method is more general in that it can be applied at arbitrary particle densities. Unlike measurement techniques based on the radial distribution function, $g(r)$, furthermore, configurational temperature

measurements can be applied to inhomogeneous systems. This new method therefore should be useful in phase separated systems at equilibrium.

We are grateful to Owen Jepps, Sven Behrens and

Brian Koss for helpful discussions. This work was supported by the Donors of the Petroleum Research Fund of the American Chemical Society.

- [1] H. H. Rugh, *Phys. Rev. Lett.* **78**, 772 (1997).
- [2] B. D. Butler, G. Ayton, O. G. Jepps, and D. J. Evans, *J. Chem. Phys.* **109**, 6519 (1998).
- [3] O. G. Jepps, G. Ayton, and E. J. Denis, *Phys. Rev. E* **62**, 4757 (2000).
- [4] G. Rickayzen and J. G. Powles, *J. Chem. Phys.* **114**, 4333 (2001).
- [5] Y. Han and G. G. Grier, *Phys. Rev. Lett.* **92**, 148301 (2004).
- [6] J. O. Hirschfelder, *J. Chem. Phys.* **33**, 1462 (1960).
- [7] G. Marc and W. G. McMillan, *Adv. Chem. Phys.* **58**, 209 (1985).
- [8] W. B. Russel, D. A. Saville, and W. R. Schowalter, *Colloidal Dispersions, Cambridge Monographs on Mechanics and Applied Mathematics* (Cambridge University Press, Cambridge, 1989).
- [9] S. H. Behrens and D. G. Grier, *J. Chem. Phys.* **115**, 6716 (2001).
- [10] J. C. Crocker and D. G. Grier, *J. Colloid Interface Sci.* **179**, 298 (1996).
- [11] J. C. Crocker, Ph.d. thesis, The University of Chicago, 1996.
- [12] S. H. Behrens and D. G. Grier, *Phys. Rev. E* **64**, 050401 (2001).
- [13] R. L. Henderson, *Phys. Lett.* **49 A**, 197 (1974).
- [14] G. M. Kepler and S. Fraden, *Phys. Rev. Lett.* **73**, 356 (1994).
- [15] R. Rajagopalan and K. S. Rao, *Phys. Rev. E* **55**, 4423 (1997).
- [16] M. D. Carbajal-Tinoco, F. Castro-Román, and J. L. Arauz-Lara, *Phys. Rev. E* **53**, 3745 (1996).
- [17] D. A. McQuarrie, *Statistical Mechanics* (University Science Books, Mill Valley, CA, 2000).
- [18] E. M. Chan, *J. Phys. C* **10**, 3477 (1977).
- [19] Y. Han and G. G. Grier, *Phys. Rev. Lett.* **91**, 038302 (2003).
- [20] J. C. Crocker and D. G. Grier, *Phys. Rev. Lett.* **77**, 1897 (1996).
- [21] J. Ennis and D. J. Evans, *Mol. Simulat.* **26**, 147 (2001).
- [22] A. Baranyai, *J. Chem. Phys.* **112**, 3964 (2000).
- [23] J. C. Crocker and D. G. Grier, *Phys. Rev. Lett.* **73**, 352 (1994).
- [24] K. Vondermassen, J. Bongers, A. Mueller, and H. Versmold, *Langmuir* **10**, 1351 (1994).